





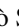


Investigating Josephson plasmons in layered cuprates via nonlinear terahertz spectroscopy

Jacopo Fiore ^{1,*}, Niccolò Sellati ¹, Francesco Gabriele ¹, Claudio Castellani ¹, Goetz Seibold ²,
Mattia Udina ¹ and Lara Benfatto ^{1,†}

¹*Department of Physics and ISC-CNR, “Sapienza” University of Rome, P.le A. Moro 5, 00185 Rome, Italy*

²*Institut für Physik, BTU Cottbus-Senftenberg, P. O. Box 101344, 03013 Cottbus, Germany*



(Received 12 January 2024; revised 8 July 2024; accepted 16 July 2024; published 6 August 2024)

Josephson plasmons in layered superconductors represent a natural source of optical nonlinearity, thanks to their intrinsically anharmonic nature. Here we derive the selection rules behind nonlinear plasmonics showing its dependence on plasmonic branches hidden to other spectroscopies, such as RIXS. We benchmark our results for the case of layered cuprates, showing how in a layered system the combined effect of plasmon dispersion and light polarization can move the resonance of the bilayer system away from the plasma edge measured in linear spectroscopy. Our results demonstrate the dependence of the nonlinear THz response on the convoluted plasmon dispersion in a momentum region complementary to RIXS, and offer a possible perspective for the generation of THz pulses by artificially designed Josephson heterostructures.

DOI: [10.1103/PhysRevB.110.L060504](https://doi.org/10.1103/PhysRevB.110.L060504)

Introduction. Plasma modes describe the propagation of longitudinal electromagnetic waves in metals, hybridized with electronic charge fluctuations. As such, they can be detected via density-sensitive probes, such as inelastic x-ray scattering [1] (RIXS) or electron energy-loss spectroscopy [2] (EELS). Whenever the metal becomes superconducting (SC) the fluctuations of the SC phase, canonically conjugated to the density, bring up the information on the plasma mode [3].

In layered superconductors, as, e.g., cuprates, the weak coupling between CuO_2 planes induces a marked anisotropy between in-plane ω_{xy} and out-of-plane ω_z long-wavelength plasma frequencies. While ω_{xy} lies at an energy scale where no appreciable change occurs across the SC transition, the soft ω_z plasmon becomes undamped by the opening of the SC gap below T_c , as evidenced by the emergence of a sharp plasma edge in the c -axis reflectivity at a temperature-dependent scale $\omega_z(T)$ [4–13]. At finite momentum the two energy scales ω_{xy} and ω_z get mixed, and the energy-momentum dispersion of the layered three-dimensional (3D) plasmon, shown in Fig. 1(a), acquires acousticlike branches at fixed k_z , see Fig. 1(b), due to the reduced screening between neighboring layers. RIXS and EELS can probe such a dispersion both in the normal and SC states, see Figs. 1(b) and 1(c), even though they cannot access the long-wavelength limit due to charge conservation [14–17].

In cuprates pair tunneling is the dominant interlayer hopping mechanism below T_c , justifying a Josephson-like description for the out-of-plane phase modes [18,19]. The excitation energy of SC Josephson plasmon scales with the cosine of the SC phase gradient. Such an intrinsic anharmonicity turns in a primary source of nonlinear optical response below T_c , thanks to the minimal coupling of the phase gradient to the gauge field [18,19]. A typical hallmark of nonlinear response

is THz third harmonic generation (THG). THG from Josephson plasmons [20–23], as well as additional effects connected to their nonlinear response [24–26], have been experimentally proven in cuprates. In analogy with nonlinear phononics [27–32], the main THG process can be understood as a sum-frequency process where two photons of the THz pulse centered at Ω excite simultaneously two plasma waves [33] with opposite 3D momenta. As a consequence, while linear reflectivity is only sensitive to the long-wavelength limits ω_{xy} , ω_z of the plasmon dispersion, nonlinear optics is sensitive to the convolution of plasmon excitations at finite momenta. This process retrieves the density of states of plasma excitations in a momentum region complementary to the one measured by RIXS, see Figs. 1(b) and 1(c), providing in principle a mechanism to selectively tune the resonance energy for THz third harmonic generation (THG) in a layered heterostructure.

Here we demonstrate this principle by comparing single- and bilayer structures. In single-layer systems, with a single plane per unit cell in the stacking direction, the light polarization projects out the full plasmon dispersion towards the low-energy ω_z value measured by linear optics. Since experiments are performed at a fixed pump frequency Ω as a function of temperature, the largest THG is expected at \bar{T} where $\Omega = \omega_z(\bar{T})$. Such a prediction, qualitatively similar to that obtained [33] by neglecting the plasmon dispersion, is consistent with experiments [20,22].

In bilayer superconductors the modulation of intralayer J_{z1} and interbilayer J_{z2} Josephson couplings along the stacking direction, with $J_{z1} \gg J_{z2}$, leads to a doubling of the Josephson plasmon branches, as originally explained in Ref. [8], giving in the long-wavelength limit two scales $\omega_{z1} \gg \omega_{z2}$. The lower one $\omega_{z2} \propto \sqrt{J_{z2}}$ controls the lower and sharper reflectivity edge at zero momentum [5–8,10–12], while the upper Josephson branch has been recently measured by RIXS [17], which turns out to be insensitive to the lower plasmon branch, see Fig. 1(c). By computing the THG for the bilayer case we show

*Contact author: jacopo.fiore@uniroma1.it

†Contact author: lara.benfatto@roma1.infn.it

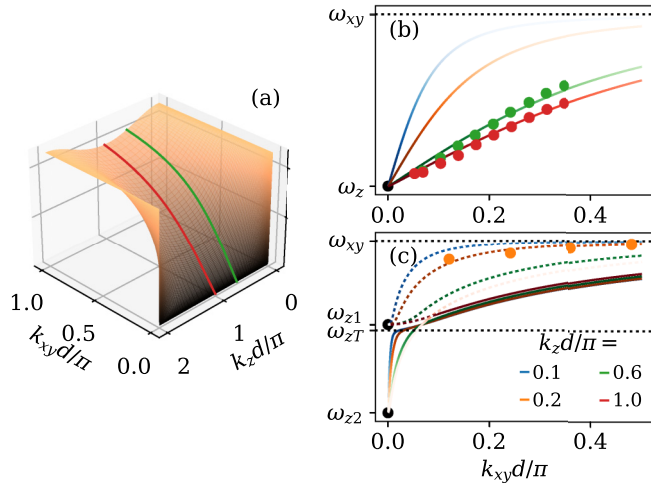


FIG. 1. (a) Plasmon dispersion in a layered superconductor from Eq. (3). Red and green solid lines highlight cuts at fixed k_z . (b) RIXS measurements (dots) from Ref. [16] superimposed to plasmon branches plotted with a line intensity proportional to the THG polarization. In the bilayer case (c) the plasmon branches (shown in log scale) double, the upper one (dashed line) being the analogous of the single-layer mode. The lower branch, which rapidly approaches the ω_T scale seen in absorption (see text), is not visible in RIXS measurements [17]. The momentum scale and color codes are the same in (b) and (c).

that the dominant contributions of plasma modes to the THG arise from intralayer phase fluctuations, scaling with the larger Josephson stiffness. As a consequence, in the bilayer system the momentum integration moves the THG spectral weight towards a higher energy scale $\omega_{zT} \approx \omega_{z1}$, explaining the lack of any resonance at the temperature \bar{T} where $\Omega = \omega_{z2}(\bar{T})$ in the measurements of Ref. [21].

Single-layer case. The contribution of plasma waves to the nonlinear optical response can be qualitatively understood within a simplified anisotropic Josephson-like model for the SC phase. Labeling with θ_n the SC phase in the n th layer one can write an effective classical Hamiltonian:

$$H = \frac{1}{8} \int d^2r d \sum_n [D_{xy}(\nabla_{xy}\theta)^2 - 8J_z \cos(\theta_{n+1} - \theta_n)], \quad (1)$$

where the in-plane phase difference has been already promoted to a continuum phase gradient, D_{xy} is the in-plane stiffness (equivalent to $\hbar^2 n_s/m$ in the continuum, isotropic limit) and J_z is an energy density defining the superfluid stiffness as $D_z = 4J_z d^2$ along the out-of-plane z direction, d being the interlayer distance. Henceforth, unless explicitly displayed, we set $\hbar = k_B = 1$. The classical model (1) is promoted to a quantum equivalent by including dynamical effects related to the phase gradient in time, scaling as $\kappa_0(\partial_\tau \theta_n)^2$, with κ_0 the charge compressibility. Once that Coulomb effects are included, κ_0 is replaced by the RPA charge compressibility [34,35]. By retaining only the quadratic term in the expansion of the cosine in Eq. (1) we obtain the following Gaussian quantum action [36–38]:

$$S_G = \frac{1}{32\pi e^2} \sum_{i\omega_m, \mathbf{k}} |\mathbf{k}|^2 [-(i\omega_m)^2 + \omega_L^2(\mathbf{k})] |\theta(i\omega_m, \mathbf{k})|^2, \quad (2)$$

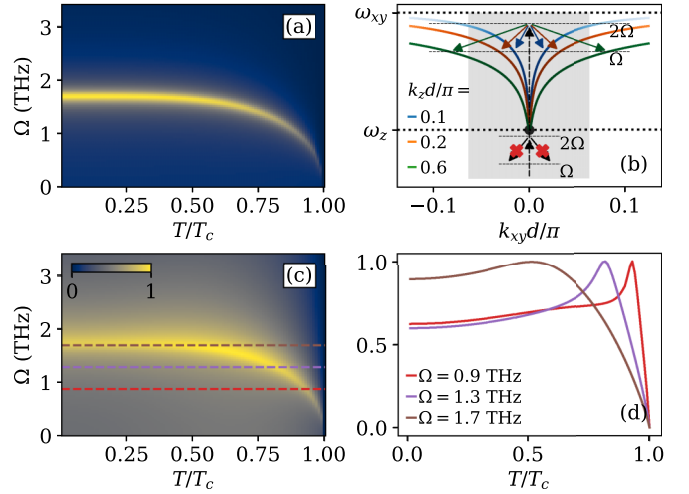


FIG. 2. Comparison between the nonlinear kernel $|K(2\Omega, T)|$ of Eq. (4) for (a) nondispersive plasmon, corresponding to replacing $\omega_L(\mathbf{k})$ with ω_z , and (c) the dispersive plasmon. (b) Sketch of the THG process. The $\omega_L(\mathbf{k})$ dispersion from Eq. (3) is plotted in log scale, with a line intensity weighted with the spectral weight of the two-plasmon process from Eq. (4). Only for $\Omega > \omega_z$ two light pulses at Ω can decay in two plasmons with opposite momenta. At larger energies the number of available states increases, but these correspond to a region with smaller spectral weight (see text and Ref. [36]). The shaded area corresponds to the region $k_{xy} < 1/\xi$ of allowed in-plane momenta. (d) $|K(2\Omega)|$ from (c) as a function of temperature for three selected pump frequencies [dashed lines in (c)], where each curve is normalized to its maximum.

where $i\omega_m = 2\pi mT$ are bosonic Matsubara frequencies, and $\omega_L(\mathbf{k})$ includes the full momentum dependence of the layered Josephson plasma mode (JPM):

$$\omega_L^2(\mathbf{k}) = \omega_{xy}^2 \frac{k_{xy}^2}{|\mathbf{k}|^2} + \omega_z^2 \frac{q_z^2}{|\mathbf{k}|^2}, \quad (3)$$

where $\omega_{xy,z}^2 = 4\pi e^2 D_{xy,z}$, $q_z = (2/d) \sin(k_z d/2)$ and $|\mathbf{k}|^2 = k_{xy}^2 + q_z^2$. An external gauge field A_z polarized along the z direction enters the model (1) via the minimal coupling substitution $\theta_{n+1} - \theta_n \rightarrow \theta_{n+1} - \theta_n - 2edA_z/c$. As detailed in the Supplemental Material [36], the third-order current $J^{NL} \sim KA_z^3$ can be obtained by expanding the cosine Josephson interaction in Eq. (1) beyond second order in the gauge-invariant phase gradient along z , and integrating out the phase degrees of freedom [33]. For a monochromatic incident field $A_z = A_0 \cos(\Omega t)$ the resulting THG intensity is proportional [39–41] to $I_{\text{THG}} \propto |K(2\Omega)|^2$. The resonant part of the nonlinear kernel K accounts for the density of states of the process involving the generation of two JPMs with opposite momenta, see Fig. 2(b), and it is given explicitly by:

$$K(\Omega) \propto J_z^2 \frac{1}{V} \sum_{\mathbf{k}} \frac{q_z^4}{|\mathbf{k}|^4} \frac{\coth(\frac{\beta\omega_L(\mathbf{k})}{2})}{\omega_L(\mathbf{k})[4\omega_L^2(\mathbf{k}) - (\Omega + i\delta)^2]}, \quad (4)$$

where $i\omega_m \rightarrow \Omega + i\delta$. Within the Josephson model (1) the coupling J_z controls both the stiffness and the anharmonic interaction terms. Thus we will adopt the same experimental temperature-dependent stiffness $D_z(T)$, $D_{xy}(T)$ both in the plasmon dispersion (3) and in the effective anharmonic

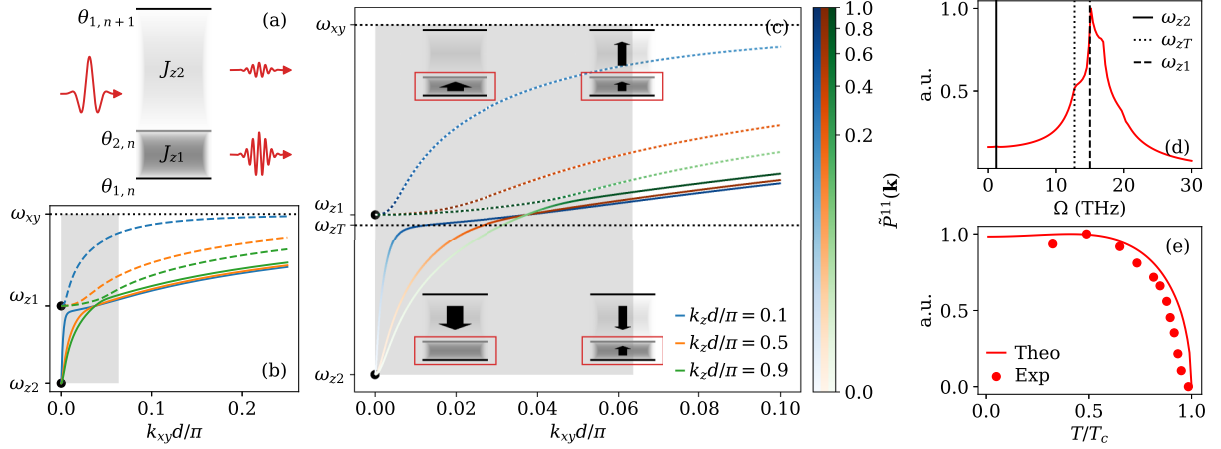


FIG. 3. (a) Sketch of the c -axis nonlinear response for the YBCO bilayer system. Since $J_{z1} \gg J_{z2}$ the THG signal is mainly determined by the intrabilayer phase fluctuations. (b) Plasmon branches $\omega_1(\mathbf{k})$ (dotted lines) and $\omega_2(\mathbf{k})$ (solid lines) at selected k_z for a wide range of k_{xy} value. (c) Zoom-in of (b) in the region of integration relevant for the THG, as denoted by the gray shaded area. Here the line intensity is rescaled according to the relative weight of intrabilayer phase fluctuations \tilde{P}_σ^{11} of each mode, shown as a color-bar on the right of the panel. A sketch of the corresponding polarizations of the modes [44] in each momenta region is also reported. (d) Frequency dependence of the nonlinear kernel $|K(2\Omega)|$ at $T = 0$. Vertical bars denote the position of ω_{z1} , ω_{zT} , and ω_{z2} . (e) Temperature dependence of the nonlinear kernel $|K(2\Omega)|$ (solid line) for fixed pump frequency $\Omega = 0.5$ THz. The dots represent the experimental data from Ref. [21].

couplings, see Refs. [36,42]. In addition, we show in the Supplemental Material [36] that the effects of the mixing [43–45] between longitudinal (plasmon) and transverse (polariton) branches below a typical scale $k_c \sim \sqrt{\omega_{xy}^2 - \omega_z^2}/c$ is quantitatively irrelevant for the THG, since the in-plane integration extends up to a much larger scale $k_{xy} \sim 1/\xi$, where $\xi \sim 5d$ is the in-plane coherence length [46,47].

In Fig. 2 we show the nonlinear kernel K as a function of temperature and frequency, by setting $\omega_{xy}(T=0) = 250$ THz and $\omega_z(T=0) = 1.7$ THz, as appropriate for optimally doped LSCO samples ($T_c = 38$ K) [22]. We compare the case where the full plasmon dispersion (3) is included [Fig. 2(c)] with the case, considered previously [33], where $\omega_L(\mathbf{k})$ is assumed to be nondispersive [Fig. 2(a)]. The latter case is equivalent to setting $\omega_L(\mathbf{k}) = \omega_z$ in Eq. (4), which results in a resonance at $\Omega = \omega_z$ of the kernel $K(2\Omega)$. As one can see, even though the dispersive case leads to a smearing of such a sharp resonance, the nonlinear kernel shows nonetheless a marked maximum around ω_z , see Fig. 2(c). The reasons are the following. As detailed in Ref. [36], the spectral weight of the two-plasmon process is zero when $\Omega < \omega_z$, with a discontinuity at the edge, which consequently causes a singularity in $|K(2\Omega = 2\omega_z)|$. Secondly, the overall factor $q_z^4/|\mathbf{k}|^4$ in Eq. (4), which accounts for the polarization of the light in the z direction, projects out the full dispersion (3) on the phase space where $q_z/|\mathbf{k}|$ is large, that corresponds to an energy around ω_z . In addition, the resonance at ω_L in Eq. (4) scales overall as $1/\omega_L^2$, highlighting further low-momentum processes, i.e., those less relevant for RIXS [14–16], see Fig. 1(b). The combined action of these effects is visualized in Fig. 2(b), where the intensity of each plasmon line is proportional to its contribution to the nonlinear kernel (4), and further discussed in the Supplemental Material [36]. The overall enhancement of the kernel at energies around ω_z leads to a nonmonotonic T dependence of the

THG measured at a fixed pump frequency $\Omega < \omega_z(T=0)$, see Fig. 2(d), maximum at \bar{T} where $\Omega = \omega_z(\bar{T})$, in qualitative agreement with the result obtained for a nondispersive plasmon [33]. Notice that even if the two-plasmon process is only possible above $2\omega_z$, the real part of the optical kernel (4) is finite below it, giving THG even when the pump frequency is below $\omega_z(T)$.

Bilayer case. In the bilayer case one has two planes denoted as $\lambda = 1, 2$ per unit cell, so that one introduces two phase variables $\theta_{\lambda,n}$. The out-of-plane Hamiltonian density is

$$\mathcal{H}_n^\perp = -J_{z1} \cos(\theta_{1,n} - \theta_{2,n}) - J_{z2} \cos(\theta_{1,n+1} - \theta_{2,n}), \quad (5)$$

in close analogy with Eq. (1), while the in-plane part has the same form. Here we introduced two different Josephson couplings J_{z1} and J_{z2} , with $J_{z1} \gg J_{z2}$, corresponding to a phase difference between the two nearest planes within the same unit cell (at distance $d_1 = 3.2 \text{ \AA}$ for YBCO) or in neighboring cells (at distance $d_2 = 8.2 \text{ \AA}$ for YBCO), $d = d_1 + d_2$ being the periodicity in the z direction [8,44,48], see Fig. 3(a). The corresponding stiffnesses $D_{z\lambda} = 4J_{z\lambda}d_\lambda^2$ are also modulated. By introducing the spinor $\bar{\theta} = (\theta_1, \theta_2)$ the generalization of the Gaussian quantum action (2) to the bilayer case reads [36]

$$S_G = \frac{1}{64\pi e^2} \sum_{i\omega_m, \mathbf{k}} \bar{\theta}(-k) \mathcal{K}^2 [-(i\omega_m)^2 \mathbb{1} + \Omega_L^2(\mathbf{k})] \bar{\theta}(k). \quad (6)$$

Here we introduced the 2×2 matrix $\mathcal{K}^2 = k_{xy}^2 \mathbb{1} + \mathcal{K}_z^\dagger \mathcal{K}_z$, which generalizes the quadratic term in momentum, where

$$\mathcal{K}_z = \frac{\sqrt{2}}{d} \begin{pmatrix} -\frac{e^{-ik_z d_1/2}}{\sqrt{d_1/d}} & \frac{e^{ik_z d_1/2}}{\sqrt{d_1/d}} \\ \frac{e^{ik_z d_2/2}}{\sqrt{d_2/d}} & -\frac{e^{-ik_z d_2/2}}{\sqrt{d_2/d}} \end{pmatrix}, \quad (7)$$

keeps track of the discretization of the phase variables along the z direction. Analogously $\Omega_L^2(\mathbf{k})$ generalizes the plasma dispersion (3), with $\Omega_L^2(\mathbf{k}) = (\mathcal{K}^2)^{-1}(\omega_{xy}^2 k_{xy}^2 \mathbb{1} + \mathcal{K}_z^\dagger \Omega_z^2 \mathcal{K}_z)$,

where $(\Omega_z^2)_{\lambda\mu} = \delta_{\lambda\mu}\omega_{z\lambda}^2$ and $\omega_{z\lambda}^2 = 4\pi e^2 D_{z\lambda}$. From the structure of Eq. (6) one readily sees that the doubling of the layers per unit cell leads to a doubling of the JPMs, defined as the square root of the eigenvalues of the matrix $\Omega_z^2(\mathbf{k})$, and shown in Fig. 3(b). The upper plasmon $\omega_1(\mathbf{k})$, dispersing between ω_{z1} and ω_{xy} , is the equivalent of the single-layer plasmon $\omega_L(\mathbf{k})$, while the additional low-energy out-of-plane plasmon $\omega_2(\mathbf{k})$, dispersing away from ω_{z2} , is characteristic of the bilayer case. For increasing in-plane momentum $\omega_2(\mathbf{k})$ evolves rapidly towards an energy scale $\omega_{zT} = \sqrt{(\omega_{z1}^2 d_2 + \omega_{z2}^2 d_1)/d} \approx \omega_{z1}$ for $J_{z1} \gg J_{z2}$, usually named transverse plasmon in the literature because it identifies the scale of a resonance peak in the c -axis optical conductivity [8,9,12]. For even larger values of k_{xy} $\omega_2(\mathbf{k})$ grows slowly towards the in-plane frequency ω_{xy} .

The computation of the nonlinear kernel follows the same steps as before, with both plasmon branches contributing to the out-of-plane response, so that $K(\Omega) = K_+(\Omega) + K_-(\Omega)$, where

$$K_{\pm}(\Omega) = \sum_{\sigma\sigma',\mathbf{k}} W_{\sigma\sigma'} \frac{\omega_{\sigma} \pm \omega_{\sigma'} \coth\left(\frac{\beta\omega_{\sigma}}{2}\right) \pm \coth\left(\frac{\beta\omega_{\sigma'}}{2}\right)}{4\omega_{\sigma}\omega_{\sigma'} (\omega_{\sigma} \pm \omega_{\sigma'})^2 - (\Omega + i\delta)^2} \quad (8)$$

combines two JPMs from the same ($\sigma = \sigma'$) or from different ($\sigma \neq \sigma'$) plasmon branches, with $\sigma, \sigma' = 1, 2$, weighted by the \mathbf{k} -dependent $W_{\sigma\sigma'}$ prefactors, which project out the contribution of each mode to selected region of momenta. A full numerical computation of the kernel (8) at $T = 0$ for parameter values appropriate for YBCO is shown in Fig. 3(d). We set $T_c = 61$ K, $\omega_{z1}(T = 0) = 15$ THz and $\omega_{z2}(T = 0) = 1.2$ THz [12,21], that gives a peak in the transverse conductivity at $\omega_{zT}(T = 0) = 11$ THz, in agreement with the experiments [12]. As one can see, $|K(2\Omega)|$ shows a marked resonance near the value $\Omega \approx \omega_{z1} \sim 15$ THz, without any signature at the lower plasmon $\omega_{z2} \sim 1.2$ THz, that is the energy scale defining instead the sharp plasma edge in the c -axis reflectivity below T_c [5,7,8,12].

A better insight into this result can be obtained by introducing a new sets of phase variables, corresponding to the intrabilayer $\tilde{\theta}_1 \sim \theta_{2,n} - \theta_{1,n}$ and interbilayer $\tilde{\theta}_2 \sim \theta_{1,n+1} - \theta_{2,n}$ phase gradient in the n th unit cell, respectively. As manifest from (5), the larger scale J_{z1} couples the gauge field A_z to $\tilde{\theta}_1$, while J_{z2} controls its coupling to $\tilde{\theta}_2$. By changing basis from (θ_1, θ_2) to $(\tilde{\theta}_1, \tilde{\theta}_2)$ one can write [36] the projectors as $W_{\sigma\sigma'} \propto \text{Tr}(\tilde{\mathcal{P}}_{\sigma} \mathcal{C} \tilde{\mathcal{P}}_{\sigma'} \mathcal{C})$, where the diagonal matrix $(\mathcal{C})_{\lambda\mu} = D_{z\lambda} d_{\lambda}^2 \delta_{\lambda\mu}$ comes from the coupling with the gauge field ($\sim D_{z\lambda} A_z^2 d_{\lambda}^2$) and the matrix $\tilde{\mathcal{P}}_{\sigma}$ weights each plasmon branch according to its projection onto interbilayer (11 element) and intrabilayer (22 element) phase fluctuations. Since $D_{z1} \gg D_{z2}$, one finds that plasmon branches contribute to THG in the momentum region where they have a large intrabilayer component, $\tilde{\mathcal{P}}_{\sigma}^{11}(\mathbf{k})$. This effect is highlighted in Fig. 3(c), where the line intensity for each plasmon dispersion, plotted at fixed k_z , scales with its $\tilde{\mathcal{P}}_{\sigma}^{11}(\mathbf{k})$ intrabilayer weight. The upper plasmon branch $\omega_1(\mathbf{k})$ is purely intrabilayer for $k_{xy} = 0$, and gradually acquires an interbilayer component as k_{xy} increases. Thus, it contributes to THG in the low-momentum region where $\omega_1(\mathbf{k}) \approx \omega_{z1}$, as already observed for the $\omega_L(\mathbf{k})$ in the single-layer case. Conversely, the lower plas-

mon branch $\omega_2(\mathbf{k})$ has exactly zero intrabilayer projection at $k_{xy} = 0$, where it is associated with purely interbilayer phase fluctuations [36,44], while it acquires intrabilayer character as it approaches the ω_{zT} energy scale. The suppression of spectral weight at low energy comes from the deep entanglement between the momentum dependence of the plasmon energies and of the polarization weights, which would not be captured if the system were described neglecting the dispersion of the plasmon branches. These two ingredients explain the lack on any signature at ω_{z2} in the numerical result of Fig. 3(d) at $T = 0$, and the absence of a THG enhancement at $\Omega = \omega_{z2}(T)$ in the THG measurements Ref. [21], performed with fixed $\Omega \sim 0.5$ THz. At the same time the condition $\Omega = \omega_{z1}(\bar{T})$ is achieved at a temperature \bar{T} so close to T_c that the resonance itself is washed out by the thermal depletion of the stiffness. Thus the computed THG, given by the solid line in Fig. 3(e), increases monotonically in temperature, in remarkable agreement with the experimental THG of Ref. [21], extracted by the measured reflected electric field E_r as [49]:

$$E_r \propto K(2\Omega) \left(\frac{2}{n(\Omega) + 1} \right)^3 \frac{1}{n(3\Omega) + n(\Omega)} \frac{1}{n(3\Omega) + 1} E_0^3, \quad (9)$$

where $n(\Omega)$ [$n(3\Omega)$] is the experimentally measured index of refraction at Ω (3Ω). Equation (9) is a modified Fresnel result, which includes also the role played by the nonlinear current [49].

Conclusions. The present results for the two-plasmon contribution to the nonlinear response reconcile experiments in single-layer and bilayer cuprates. The combined effect of the light polarization and the plasmon dispersion explains a resonant THG for pumping frequency matching the plasma edge in single-layer materials, while it accounts for a shift of the resonance frequency towards the larger out-of-plane plasma mode for bilayer structures. It turns out that in those systems THG is sensitive exactly to the part of the plasmon branches that are hidden to RIXS, as shown in Fig 1(c), where recent RIXS measurements from Ref. [17] have been reported. Even though such a dichotomy is not yet understood theoretically [17], we expect that it should come from different selection rules at play for the plasma-mode contribution to the current (probed by THG) or to the density (probed by RIXS) response.

On a more general perspective, the present results can serve as a guide to engineer artificial heterostructures for the generation of THz pulses via THG up conversion, using the plasmon dispersion to tune the enhancement of the nonlinear response for pumping THz field polarized along the layer stacking direction in cuprate superconductors. In the last few years giant progresses have been made in the realization of stable superconducting films of Bi-based cuprates, down to the dimensions of few unit cells [50–52]. It is now possible to realize efficient and tunable Josephson junctions by twisting neighboring films, thanks to the angle dependence of the pair tunneling in a d -wave superconductor [53–55]. Even though the present technology is still limited to single junctions, in the near future the realization of Junction arrays could lead to controllable artificial bilayer lattices, with a tunable resonance frequency. At the same time, the full quantum description of the nonlinear Josephson response is the starting point for

the understanding of the multidimensional spectrum obtained in two-dimensional THz protocols [26], and to assess its potential for disentangling the intrinsic thermal effects from inhomogeneity broadening in unconventional cuprates.

Acknowledgments. We acknowledge K. Katsumi and N. Poccia for useful discussions. We thank K. Katsumi for

providing us with the experimental data from Ref. [21]. We acknowledge financial support by European Community by ERC-SYN MORE-TEM G.A. No 951215 and by Sapienza University via Ateneo 2021 (RM12117A4A7FD11B), Ateneo 2022 (RP1221816662A977), and Ateneo 2023 (RM123188E357C540).

- [1] L. J. P. Ament, M. van Veenendaal, T. P. Devereaux, J. P. Hill, and J. van den Brink, Resonant inelastic x-ray scattering studies of elementary excitations, *Rev. Mod. Phys.* **83**, 705 (2011).
- [2] F. J. García de Abajo, Optical excitations in electron microscopy, *Rev. Mod. Phys.* **82**, 209 (2010).
- [3] N. Nagaosa, *Quantum Field Theory in Condensed Matter Physics* (Springer, Berlin, 1999)
- [4] K. Tamasaku, Y. Nakamura, and S. Uchida, Charge dynamics across the CuO₂ planes in La_{2-x}Sr_xCuO₄, *Phys. Rev. Lett.* **69**, 1455 (1992).
- [5] C. C. Homes, T. Timusk, R. Liang, D. A. Bonn, and W. N. Hardy, Optical conductivity of c axis oriented YBa₂Cu₃O_{6.70}: Evidence for a pseudogap, *Phys. Rev. Lett.* **71**, 1645 (1993).
- [6] J. H. Kim, H. S. Somal, M. T. Czyzyk, D. van der Marel, A. Wittlin, A. M. Gerrits, V. H. M. Duijn, N. T. Hien, and A. A. Menovsky, Strong damping of the c-axis plasmon in high-T_c cuprate superconductors, *Physica C: Supercond.* **247**, 297 (1995).
- [7] D. N. Basov, T. Timusk, B. Dabrowski, and J. D. Jorgensen, C-axis response of YBa₂Cu₄O₈: A pseudogap and possibility of Josephson coupling of CuO₂ planes, *Phys. Rev. B* **50**, 3511 (1994).
- [8] D. van der Marel and A. Tsvetkov, Transverse optical plasmons in layered superconductors, *Czech. J. Phys.* **46**, 3165 (1996).
- [9] D. Munzar, C. Bernhard, A. Golnik, J. Humlíček, and M. Cardona, Anomalies of the infrared-active phonons in underdoped YBa₂Cu₃O_y as evidence for the intra-bilayer Josephson effect, *Solid State Commun.* **112**, 365 (1999).
- [10] T. Kakeshita, S. Uchida, K. M. Kojima, S. Adachi, S. Tajima, B. Gorshunov, and M. Dressel, Transverse josephson plasma mode in T* cuprate superconductors, *Phys. Rev. Lett.* **86**, 4140 (2001).
- [11] D. Dulić, A. Pimenov, D. van der Marel, D. M. Broun, S. Kamal, W. N. Hardy, A. A. Tsvetkov, I. M. Sutjaha, R. Liang, A. A. Menovsky, A. Loidl, and S. S. Saxena, Observation of the transverse optical plasmon in SmLa_{0.8}Sr_{0.2}CuO_{4-δ}, *Phys. Rev. Lett.* **86**, 4144 (2001).
- [12] W. Hu, S. Kaiser, D. Nicoletti, C. R. Hunt, I. Gierz, M. C. Hoffmann, M. Le Tacon, T. Loew, B. Keimer, and A. Cavalleri, Optically enhanced coherent transport in YBa₂Cu₃O_{6.5} by ultrafast redistribution of interlayer coupling, *Nature Mater.* **13**, 705 (2014).
- [13] S. V. Dordevic, S. Komiya, Y. Ando, and D. N. Basov, Josephson plasmon and inhomogeneous superconducting state in La_{2-x}Sr_xCuO₄, *Phys. Rev. Lett.* **91**, 167401 (2003).
- [14] M. Hepting, L. Chaix, E. W. Huang, R. Fumagalli, Y. Y. Peng, B. Moritz, K. Kummer, N. B. Brookes, W. C. Lee, M. Hashimoto, T. Sarkar, J.-F. He, C. R. Rotundu, Y. S. Lee, R. L. Greene, L. Braicovich, G. Ghiringhelli, Z. X. Shen, T. P. Devereaux, and W. S. Lee, Three-dimensional collective charge excitations in electron-doped copper oxide superconductors, *Nature (London)* **563**, 374 (2018).
- [15] J. Lin, J. Yuan, K. Jin, Z. Yin, G. Li, K.-J. Zhou, X. Lu, M. Dantz, T. Schmitt, H. Ding, H. Guo, M. P. M. Dean, and X. Liu, Doping evolution of the charge excitations and electron correlations in electron-doped superconducting La_{2-x}Ce_xCuO₄, *npj Quantum Mater.* **5**, 4 (2020).
- [16] A. Nag, M. Zhu, M. Bejas, J. Li, H. C. Robarts, H. Yamase, A. N. Petsch, D. Song, H. Eisaki, A. C. Walters, M. García-Fernández, A. Greco, S. M. Hayden, and K.-J. Zhou, Detection of acoustic plasmons in hole-doped lanthanum and bismuth cuprate superconductors using resonant inelastic X-ray scattering, *Phys. Rev. Lett.* **125**, 257002 (2020).
- [17] M. Bejas, V. Zimmermann, D. Betto, T. D. Boyko, R. J. Green, T. Loew, N. B. Brookes, G. Cristiani, G. Logvenov, M. Minola, B. Keimer, H. Yamase, A. Greco, and M. Hepting, Plasmon dispersion in bilayer cuprate superconductors, *Phys. Rev. B* **109**, 144516 (2024).
- [18] S. Savel'ev, V. A. Yampol'skii, A. L. Rakhmanov, and F. Nori, Terahertz Josephson plasma waves in layered superconductors: Spectrum, generation, nonlinear and quantum phenomena, *Rep. Prog. Phys.* **73**, 026501 (2010).
- [19] S. Savel'ev, A. L. Rakhmanov, V. A. Yampol'skii, and F. Nori, Analogues of nonlinear optics using terahertz Josephson plasma waves in layered superconductors, *Nature Phys.* **2**, 521 (2006).
- [20] S. Rajasekaran, J. Okamoto, L. Mathey, M. Fechner, V. Thampy, G. D. Gu, and A. Cavalleri, Probing optically silent superfluid stripes in cuprates, *Science* **359**, 575 (2018).
- [21] K. Katsumi, M. Nishida, S. Kaiser, S. Miyasaka, S. Tajima, and R. Shimano, Near-infrared light-induced superconducting-like state in underdoped YBa₂Cu₃O_y studied by c-axis Terahertz third-harmonic generation, *Phys. Rev. B* **107**, 214506 (2023).
- [22] K. Kaj, K. A. Cremin, I. Hammock, J. Schalch, D. N. Basov, and R. D. Averitt, Terahertz third harmonic generation in c-axis La_{1.85}Sr_{0.15}CuO₄, *Phys. Rev. B* **107**, L140504 (2023).
- [23] S. Zhang, Z. Sun, Q. Liu, Z. Wang, Q. Wu, L. Yue, S. Xu, T. Hu, R. Li, X. Zhou, J. Yuan, G. Gu, T. Dong, and N. Wang, Revealing the frequency-dependent oscillations in nonlinear Terahertz response induced by Josephson current, *Natl. Sci. Rev.*, **10** nwad163 (2023).
- [24] Y. Laplace and A. Cavalleri, Josephson plasmonics in layered superconductors, *Adv. Phys.: X* **1**, 387 (2016).
- [25] D. Fu, D. Nicoletti, M. Fechner, M. Buzzi, G. D. Gu, and A. Cavalleri, Terahertz phase slips in striped La_{2-x}Ba_xCuO₄, *Phys. Rev. B* **105**, L020502 (2022).
- [26] A. Liu, D. Pavicevic, M. H. Michael, A. G. Salvador, P. E. Dolgirev, M. Fechner, A. S. Disa, P. M. Lozano, Q. Li, G. D. Gu, E. Demler, and A. Cavalleri, Probing inhomogeneous

- cuprate superconductivity by terahertz Josephson echo spectroscopy, [arXiv:2308.14849](https://arxiv.org/abs/2308.14849) [cond-mat, physics:physics].
- [27] D. M. Juraschek and S. F. Maehrlein, Sum-frequency ionic Raman scattering, *Phys. Rev. B* **97**, 174302 (2018).
- [28] A. von Hoegen, R. Mankowsky, M. Fechner, M. Först, and A. Cavalleri, Probing the interatomic potential of solids with strong-field nonlinear phononics, *Nature (London)* **555**, 79 (2018).
- [29] M. Först, C. Manzoni, S. Kaiser, Y. Tomioka, Y. Tokura, R. Merlin, and A. Cavalleri, Nonlinear phononics as an ultrafast route to lattice control, *Nature Phys.* **7**, 854 (2011).
- [30] A. Subedi, A. Cavalleri, and A. Georges, Theory of nonlinear phononics for coherent light control of solids, *Phys. Rev. B* **89**, 220301(R) (2014).
- [31] X. Li, T. Qiu, J. Zhang, E. Baldini, J. Lu, A. M. Rappe, and K. A. Nelson, Terahertz field-induced ferroelectricity in quantum paraelectric SrTiO₃, *Science* **364**, 1079 (2019).
- [32] M. Basini, M. Udina, M. Pancaldi, V. Unikandanunni, S. Bonetti, and L. Benfatto, Terahertz ionic Kerr effect: Two-phonon contribution to the nonlinear optical response in insulators, *Phys. Rev. B* **109**, 024309 (2024).
- [33] F. Gabriele, M. Udina, and L. Benfatto, Non-linear Terahertz driving of plasma waves in layered cuprates, *Nature Commun.* **12**, 752 (2021).
- [34] L. Benfatto, A. Toschi, and S. Caprara, Low-energy phase-only action in a superconductor: A comparison with the XY model, *Phys. Rev. B* **69**, 184510 (2004).
- [35] Z. Sun, M. M. Fogler, D. N. Basov, and A. J. Millis, Collective modes and terahertz near-field response of superconductors, *Phys. Rev. Res.* **2**, 023413 (2020).
- [36] See Supplemental Material at <http://link.aps.org/supplemental/10.1103/PhysRevB.110.L060504> for extended calculations and further discussion.
- [37] A. Paramekanti, M. Randeria, T. V. Ramakrishnan, and S. S. Mandal, Effective actions and phase fluctuations in d-wave superconductors, *Phys. Rev. B* **62**, 6786 (2000).
- [38] S. De Palo, C. Castellani, C. Di Castro, and B. K. Chakraverty, Effective action for superconductors and BCS-Bose crossover, *Phys. Rev. B* **60**, 564 (1999).
- [39] T. Cea, C. Castellani, and L. Benfatto, Nonlinear optical effects and third-harmonic generation in superconductors: Cooper pairs versus Higgs mode contribution, *Phys. Rev. B* **93**, 180507(R) (2016).
- [40] M. Udina, T. Cea, and L. Benfatto, Theory of coherent-oscillations generation in Terahertz pump-probe spectroscopy: From phonons to electronic collective modes, *Phys. Rev. B* **100**, 165131 (2019).
- [41] G. Seibold, M. Udina, C. Castellani, and L. Benfatto, Third harmonic generation from collective modes in disordered superconductors, *Phys. Rev. B* **103**, 014512 (2021).
- [42] T. Shibauchi, H. Kitano, K. Uchinokura, A. Maeda, T. Kimura, and K. Kishio, Anisotropic penetration depth in La_{2-x}Sr_xCuO₄, *Phys. Rev. Lett.* **72**, 2263 (1994).
- [43] F. Gabriele, C. Castellani, and L. Benfatto, Generalized plasma waves in layered superconductors: A unified approach, *Phys. Rev. Res.* **4**, 023112 (2022).
- [44] N. Sellati, F. Gabriele, C. Castellani, and L. Benfatto, Generalized Josephson plasmons in bilayer superconductors, *Phys. Rev. B* **108**, 014503 (2023).
- [45] F. Gabriele, R. Senese, C. Castellani, and L. Benfatto, Charge-density response in layered metals: Retardation effects, generalized plasma waves, and their spectroscopic signatures, *Phys. Rev. B* **109**, 045137 (2024).
- [46] Y. Ando and K. Segawa, Magnetoresistance of untwinned YBa₂Cu₃O_y single crystals in a wide range of doping: Anomalous hole-doping dependence of the coherence length, *Phys. Rev. Lett.* **88**, 167005 (2002).
- [47] M. Suzuki and M. Hikita, Resistive transition, magnetoresistance, and anisotropy in La_{2-x}Sr_xCuO₄ single-crystal thin films, *Phys. Rev. B* **44**, 249 (1991).
- [48] F. Alpeggiani and L. C. Andreani, Josephson surface plasmons in spatially confined cuprate superconductors, *Phys. Rev. B* **88**, 174513 (2013).
- [49] J. Fiore (unpublished).
- [50] Y. Yu, L. Ma, P. Cai, R. Zhong, C. Ye, J. Shen, G. D. Gu, X. H. Chen, and Y. Zhang, High-temperature superconductivity in monolayer Bi₂Sr₂CaCu₂O_{8+δ}, *Nature (London)* **575**, 156 (2019).
- [51] S. Y. F. Zhao, N. Poccia, M. G. Panetta, C. Yu, J. W. Johnson, H. Yoo, R. Zhong, G. D. Gu, K. Watanabe, T. Taniguchi, S. V. Postolova, V. M. Vinokur, and P. Kim, Sign-reversing hall effect in atomically thin high-temperature Bi_{2,1}Sr_{1,9}CaCu_{2,0}O_{8+δ} superconductors, *Phys. Rev. Lett.* **122**, 247001 (2019).
- [52] N. Poccia, S. Y. F. Zhao, H. Yoo, X. Huang, H. Yan, Y. S. Chu, R. Zhong, G. Gu, C. Mazzoli, K. Watanabe, T. Taniguchi, G. Campi, V. M. Vinokur, and P. Kim, Spatially correlated incommensurate lattice modulations in an atomically thin high-temperature Bi_{2,1}Sr_{1,9}CaCu_{2,0}O_{8+y} superconductor, *Phys. Rev. Mater.* **4**, 114007 (2020).
- [53] S. Y. F. Zhao, X. Cui, P. A. Volkov, H. Yoo, S. Lee, J. A. Gardener, A. J. Akey, R. Engelke, Y. Ronen, R. Zhong, G. Gu, S. Plugge, T. Tummuru, M. Kim, M. Franz, J. H. Pixley, N. Poccia, and P. Kim, Time-reversal symmetry breaking superconductivity between twisted cuprate superconductors, *Science* **382**, 1422 (2023).
- [54] Y. Lee, M. Martini, T. Confolone, S. Shokri, C. N. Saggau, D. Wolf, G. Gu, K. Watanabe, T. Taniguchi, D. Montemurro, V. M. Vinokur, K. Nielsch, and N. Poccia, Encapsulating high-temperature superconducting twisted van der Waals heterostructures blocks detrimental effects of disorder, *Adv. Mater.* **35**, 2209135 (2023).
- [55] M. Martini, Y. Lee, T. Confolone, S. Shokri, C. N. Saggau, D. Wolf, G. Gu, K. Watanabe, T. Taniguchi, D. Montemurro, V. M. Vinokur, K. Nielsch, and N. Poccia, Twisted cuprate van der Waals heterostructures with controlled Josephson coupling, *Mater. Today* **67**, 106 (2023).